
MedSeg-R: Medical Image Segmentation with Clinical Reasoning

Hao Shao*, Qibin Hou[†]

VCIP, School of Computer Science, Nankai University

Project page: <https://github.com/haoshao-nku/MedSeg-R.git>

Abstract

Medical image segmentation is challenging due to overlapping anatomies with ambiguous boundaries and a severe imbalance between the foreground and background classes, which particularly affects the delineation of small lesions. Existing methods, including encoder–decoder networks and prompt-driven variants of the Segment Anything Model (SAM), rely heavily on local cues or user prompts and lack integrated semantic priors, thus failing to generalize well to low-contrast or overlapping targets. To address these issues, we propose MedSeg-R, a lightweight, dual-stage framework inspired by clinical reasoning. Its cognitive stage interprets medical report into structured semantic priors (location, texture, shape), which are fused via transformer block. In the perceptual stage, these priors modulate the SAM backbone: spatial attention highlights likely lesion regions, dynamic convolution adapts feature filters to expected textures, and deformable sampling refines spatial support. By embedding this fine-grained guidance early, MedSeg-R disentangles inter-class confusion and amplifies minority-class cues, greatly improving sensitivity to small lesions. In challenging benchmarks, MedSeg-R produces large Dice improvements in overlapping and ambiguous structures, demonstrating plug-and-play compatibility with SAM-based systems.

1 Introduction

Medical image segmentation is a cornerstone of numerous clinical workflows, enabling the precise delineation of organs, lesions, and anatomical structures across imaging modalities such as CT, MRI, and X-ray [Ma et al. \[2022\]](#), [Shao et al. \[2024\]](#), [Gaggion et al. \[2022\]](#). Its pixel-level accuracy underpins a range of critical downstream tasks, including quantitative analysis, radiotherapy planning, and longitudinal disease monitoring [Schipaanboord et al. \[2019\]](#), [Iqbal et al. \[2023\]](#). Despite substantial progress, two persistent challenges continue to hinder robust and generalizable segmentation: (1) inter-class overlap, where spatially adjacent anatomical regions exhibit highly similar intensity and texture patterns, resulting in ambiguous boundaries; and (2) small object segmentation, where extreme class imbalance leads to underrepresentation and unreliable detection of subtle but clinically significant findings.

Early convolutional models, including U-Net [Ronneberger et al. \[2015\]](#) and its attention-based [Oktay et al. \[2018\]](#), improve multi-scale feature integration but are still limited by local receptive fields. Subsequent Transformer-based methods [Chen et al. \[2021\]](#), [Zheng et al. \[2021\]](#) introduce global context modeling, improving anatomical reasoning. However, both families of methods still struggle with overlapping structures and small objects.

*Email at shaoh@mail.nankai.edu.cn

[†]Corresponding authors, email at: houbq@nankai.edu.cn

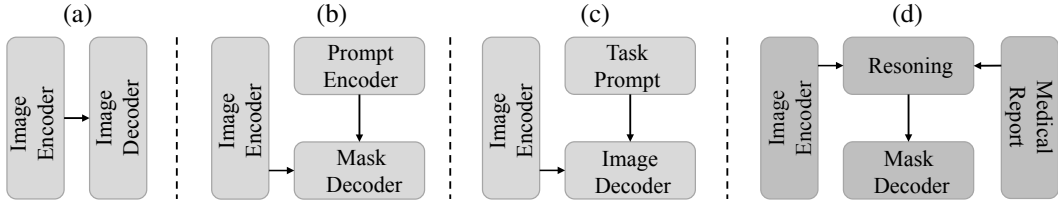


Figure 1: Comparison of MedSeg-R with existing approaches. (a) CNN/Transformer-based models, (b) prompt-driven SAM variants, (c) cross-dataset learning methods, and (d) our MedSeg-R. Different from others, MedSeg-R adopts a unique two-stage paradigm inspired by clinical reasoning, where structured priors (e.g., location, texture, shape) explicitly guide the visual feature extraction process.

To pursue more generalizable medical image segmentation, two prominent paradigms have emerged: **prompt-driven modeling** and **cross-dataset learning**. The first paradigm, **prompt-driven modeling**, is exemplified by the Segment Anything Model (SAM), which introduces a flexible prompt-based segmentation mechanism with strong generalization capabilities. Its medical adaptations, such as MedSAM Ma et al. [2024] and SAM-Med2D Cheng et al. [2023], leverage domain-specific fine-tuning to deliver promising results across diverse medical imaging tasks. However, these models still rely heavily on explicit prompts and lack semantic reasoning capabilities, limiting their performance in scenarios involving ambiguous boundaries or subtle lesions. The second paradigm, **cross-dataset learning**, is represented by frameworks such as UniSeg Ye et al. [2023] and UniverSeg Butoi et al. [2023], which aim to generalize across modalities and anatomical targets via large-scale, cross-domain training. Although effective in reducing overfitting to specific datasets, these models remain susceptible to domain shifts, require substantial manual annotation, and struggle with semantic ambiguity and class imbalance—especially in the case of small or overlapping structures.

All prevailing segmentation paradigms, including convolutional, Transformer-based, prompt driven, and cross-dataset methods, share a fundamental flaw: They are difficult to fully exploit structured clinical priors, such as organ location, characteristic texture patterns, and lesion shapes, throughout the processing pipeline. They are mainly based on raw image features as shown in Fig. 1. In contrast, clinicians interpret medical images using extensive prior knowledge. Even before identifying a structure, they recall expected anatomical locations, typical tissue appearances, and the morphological signatures of common pathologies. These structured priors guide their attention to diagnostically relevant regions, enabling them to resolve overlapping boundaries and detect subtle abnormalities that purely image-driven approaches often overlook.

SEG-SAM Huang et al. [2024] takes a meaningful step toward leveraging clinical priors by introducing structured textual cues such as object location, object texture patterns, and object shapes through a dual-decoder design. However, it encodes this information as a single global sentence embedding, offering only coarse semantic guidance. The added decoder also increases the complexity of the system without directly improving the feature representation process. As a result, SEG-SAM underutilizes fine-grained priors.

Motivated by the need to better utilize structured clinical priors, we propose MedSeg-R, a two-stage framework tailored for medical image segmentation as shown in Fig 2. Unlike SEG-SAM Huang et al. [2024], which encodes prior knowledge into a single global sentence vector, our method focuses on how to fully utilize fine-grained priors, such as object location, object texture patterns, and object shapes, while avoiding additional architectural complexity. Specifically, MedSeg-R adopts a two-stage design inspired by clinical reasoning. In the cognitive stage, it parses radiology-style descriptions into structured semantic attributes and fuses them via cross-attention into a unified prior. In the perceptual stage, this prior adaptively modulates the visual backbone of SAM, directing attention to the likely anatomical regions, enhancing the sensitivity to expected textures and aligning the receptive fields with the morphology of the lesion. By embedding fine-grained guidance directly into the feature extraction process, MedSeg-R avoids redundant decoding paths while improving segmentation accuracy for small, ambiguous, and overlapping structures. Our contributions are three-fold.

- We propose a novel two-stage segmentation paradigm inspired by clinical reasoning, consisting of a cognitive stage that parses diagnostic descriptions into structured semantic attributes and a perceptual stage that uses these attributes to guide feature extraction and resolve ambiguities in complex anatomical boundaries.

- We design lightweight and interpretable modules that inject structured clinical priors into the SAM backbone via attention and dynamic convolution mechanisms, enhancing segmentation accuracy for small and overlapping structures.
- We demonstrate that MedSeg-R significantly outperforms state-of-the-art SAM-based methods across overlapping and small-object scenarios. On the SAM-Med2D benchmark, it achieves consistent gains under both point and box prompts, improving small-object Dice scores by up to **+1.99%** and **+1.76%**, respectively. Furthermore, MedSeg-R maintains superior performance even without any prompts, confirming its strong generalization and reduced reliance on external guidance. On the Synapse dataset, it outperforms SEG-SAM by **+2.62%** in overall Dice, with substantial improvements on challenging organs like the gallbladder (**+5.03%**) and pancreas (**+2.22%**).

2 Related Work

Traditional medical image segmentation. Medical image segmentation requires balancing fine-grained boundary delineation with global semantic consistency, particularly in the presence of anatomical overlap and small lesions. U-Net [Ronneberger et al. \[2015\]](#) pioneers encoder-decoder architectures with skip connections, forming the basis for numerous subsequent methods. Enhancements such as Attention U-Net [Oktay et al. \[2018\]](#) and UNet++ [Zhou et al. \[2018\]](#) introduce attention mechanisms and nested connectivity to improve feature integration and localization. Volumetric variants like 3D U-Net [Çiçek et al. \[2016\]](#) and nnU-Net [Isensee et al. \[2018\]](#) extend segmentation to 3D modalities, enabling context-aware predictions across slices. However, the above models share inherent limitations: Their fixed receptive fields constrain long-range dependency modeling, and their performance deteriorates in regions with low contrast or overlapping anatomical structures. Transformer-based architectures [Vaswani et al. \[2017\]](#) mitigate these limitations by introducing global self-attention. TransUNet [Chen et al. \[2021\]](#) combines CNN encoders with Transformer modules to fuse local and global information, while SETR [Zheng et al. \[2021\]](#) explored pure transformer decoders. Subsequent models like CoTr [Xie et al. \[2021\]](#), TransBTS [Wenxuan et al. \[2021\]](#), and Swin-UNet [Cao et al. \[2022\]](#) further advance spatial coherence and multi-scale representation. However, these methods still have difficulties in handling fine-grained object boundaries and small object sensitivity due to insufficient supervision and over-smoothing of representations.

Universal medical segmentation. To promote generalization across organs and modalities, one of the paradigms of universal segmentation frameworks is to learn shared representations through cross-task training. UniSeg [Ye et al. \[2023\]](#) and UniverSeg [Butoi et al. \[2023\]](#) achieve cross-dataset generalization by aligning anatomy-aware features through multi-domain supervision, enabling zero-shot segmentation of unseen structures. However, their reliance on large-scale labeled corpora and their vulnerability to domain shifts limit real-world applicability. To improve task-awareness, Iris [Gao et al. \[2025\]](#) introduces a reference-guided framework that extracts relevant semantics from support examples. However, its dependence on high-quality references reduces robustness in low-resource settings or under noisy annotations. In volumetric contexts, 3DU²-Net [Huang et al. \[2019\]](#) and S2VNet [Ding et al. \[2024\]](#) introduce architectural strategies to reduce redundancy and memory costs through separable convolutions or centroid-guided propagation. These methods struggle to maintain accurate lesion boundaries across slices.

SAM adaptation in medical imaging. Prompt-driven modeling, exemplified by the Segment Anything Model (SAM), has become a prominent approach for medical image segmentation. Initial adaptations like Med-SA [Wu et al. \[2025\]](#) and SAM-Med2D [Cheng et al. \[2023\]](#) show that lightweight fine-tuning on medical datasets can achieve competitive multi-organ performance. However, their reliance on manual or heuristic prompts and the lack of integrated semantic reasoning limit their effectiveness in complex scenarios. To improve semantic guidance, MedCLIP-SAM [Koleilat et al. \[2024\]](#) integrates CLIP-derived embeddings, enabling text-driven segmentation with gScoreCAM [Chen et al. \[2022\]](#). However, the coarse and noisy nature of its language priors compromises localization accuracy. Approaches like TP-DRSeg [Li et al. \[2024\]](#) and OMT-SAM [Zhang et al. \[2025\]](#) sight better alignment between vision and language embeddings, but they require extensive paired training data and showed limited generalization to unseen variations. Volumetric extensions such as SAM-Med3D [Wang et al. \[2023\]](#) preserve most of SAM’s weights while introducing spatial adapters for improved performance on tasks like pancreatic tumor segmentation. Similarly, OpenVocabCT [Li et al.](#)

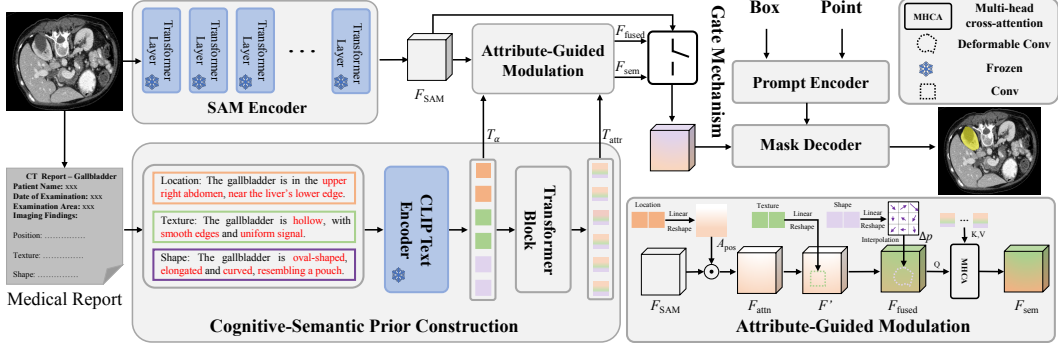


Figure 2: Overview of the MedSeg-R framework. The input image features from SAM’s encoder are first guided by clinical priors (organ location/texture/shape) in the cognitive stage and then boundary-optimized in the perceptual stage. A gating mechanism fuses these refined features with the original SAM features and clinical guidance. The output is fed into SAM’s mask decoder with prompt inputs to produce precise segmentation.

[2025] leverages radiology reports for open-vocabulary CT segmentation but struggle with aligning text to voxel-level granularity.

The above SAM-based methods all have an inherent defect: It is difficult to fully utilize structured clinical prior knowledge in the entire processing flow. Our proposed **MedSeg-R** fills this gap by introducing structured, attribute-level priors in a cognitively inspired pipeline, enhancing lesion segmentation performance under inter-class ambiguity and class imbalance.

3 Method

To better leverage structured clinical prior knowledge, we propose MedSeg-R, a two-stage framework that extracts fine-grained semantic priors (such as organ location, texture, and shape) from clinical text. This multi-level and fine-grained guidance enhances MedSeg-R’s ability to resolve inter-class overlap and improve small-object segmentation accuracy.

3.1 Framework of MedSeg-R

The overall framework of MedSeg-R is illustrated in Fig. 2. Given an input image I , it is first passed through the SAM image encoder to extract feature representations. These features are then processed through two key stages of refinement: the **cognitive** stage and the **perceptual** stage. In the cognitive stage, structured semantic priors, such as organ location, texture, and shape, are extracted and integrated to provide high-level guidance for the feature refinement process. In the perceptual stage, these priors modulate the feature representations, enabling fine-grained adjustments to the segmentation boundaries.

After passing through these two stages, the refined features, semantic priors, and the output from SAM’s image encoder are fused using a gating mechanism. This mechanism combines the refined features, the SAM encoder output, and the semantic priors to produce an enhanced representation. Finally, this fused information is combined with the input from the prompt encoder and passed into SAM’s mask decoder, which generates the final segmentation result. This two-stage refinement process, coupled with the gating mechanism, allows for more accurate segmentation, particularly for small or ambiguous objects, by effectively utilizing structured clinical priors throughout the feature extraction pipeline, which will be shown in the experiment section.

3.2 Stage I: Cognitive-Semantic Prior Construction.

In the cognitive stage, we replicate the way clinicians form a high-level understanding of anatomy before closely inspecting the image. This stage involves extracting key semantic information from clinical reports to guide the subsequent analysis. We begin by breaking the clinical report into three key attribute texts that represent critical aspects of anatomy: $T_{\text{pos}}^{\text{txt}}$, $T_{\text{tex}}^{\text{txt}}$, and $T_{\text{shape}}^{\text{txt}}$, which correspond to anatomical location, texture patterns, and object morphology. These attributes help clinicians

understand the lesion’s position, appearance, and form. Each attribute text is then encoded using CLIP’s text encoder into token embeddings. This process mirrors how clinicians mentally categorize key attributes, such as location, texture, and shape, before they begin inspecting the image in detail.

After encoding, the three attribute embeddings are combined and processed using the cross-attribute attention, which can be implemented with a Transformer block to refine each attribute by leveraging the context provided by the others. For example, a clinician’s understanding of the shape of a lesion may influence their interpretation of its texture. This integrated representation helps to create a more cohesive understanding of the anatomy. Finally, the fused tokens are aggregated into a single semantic prior vector using average pooling. This vector encapsulates the clinical hypothesis, which will guide the subsequent stages of image analysis. The calculation formulas for this process are as follows:

$$T_\alpha = \text{CLIP}_{\text{text}}(T_\alpha^{\text{txt}}) \in \mathbb{R}^{L_\alpha \times d}, \quad \text{for } \alpha \in \{\text{pos}, \text{tex}, \text{shape}\}, \quad (1)$$

$$T_{\text{cross}} = \text{TransformerBlock}([T_{\text{pos}}; T_{\text{tex}}; T_{\text{shape}}]) \in \mathbb{R}^{(L_{\text{pos}}+L_{\text{tex}}+L_{\text{shape}}) \times d}, \quad (2)$$

$$T_{\text{attr}} = \text{AvePool}(T_{\text{cross}}) \in \mathbb{R}^{1 \times d}. \quad (3)$$

In this formula, L_α represents the sequence length of the input text T_α^{txt} , which corresponds to the number of tokens in the text after tokenization, and d refers to the embedding dimension, which is the length of the vector representation for each token generated by the CLIP encoder. AvePool represents the average pooling operation.

3.3 Stage II: Perceptual-Attribute-Guided Modulation

In the perceptual stage, MedSeg-R first uses the features of location, texture, and shape extracted through the CLIP text encoder to guide the output of SAM’s image encoder. Each attribute cue plays a specific role. Positional cues help focus attention on relevant regions, texture cues adapt the filters to highlight object-specific patterns, and shape cues guide spatial sampling to accurately trace the contours of the target regions. The guided output is modulated by the semantic prior vector T_{attr} constructed in the cognitive stage to refine object features.

Given the feature output F_{SAM} with spatial size $H \times W$ from SAM’s image encoder and $T_\alpha, \alpha \in \{\text{pos}, \text{tex}, \text{shape}\}$ from the output of CLIP text encoder, we first extract the positional prior T_{pos} . This positional prior T_{pos} is first flatten and then linearly projected to a spatial attention map $A_{\text{pos}} \in H \times W$ after the reshape operation. Then, A_{pos} is operated on each channel of F_{SAM} , yielding F_{attn} . This influences the encoder’s focus, helping suppress irrelevant background responses. In addition, it ensures that the processing focuses on clinically relevant regions, particularly those that clinicians would typically prioritize.

Next, we use the texture priors T_{tex} to adjust the resulting F_{attn} , which is tailored to produce imaging characteristics. Given T_{tex} , we first flatten it to a 1D vector and then project it to a 7×7 matrix via linear projection. The resulting 7×7 matrix is used as a convolutional filter to perform convolution with each channel of F_{attn} , yielding F' . By doing so, MedSeg-R amplifies subtle object signals that generic filters might overlook. Finally, we use a deformable convolution Dai et al. [2017] to encode the shape priors T_{shape} . T_{shape} is first flatten and then sent into a linear layer to generate kernels and offsets Δp , which will then be used in the deformable convolution as done in Gong et al. [2021] to refine spatial sampling according to the expected lesion morphology, yielding F_{fused} . This step ensures that the receptive fields align with the anticipated object form, which is helpful for improving boundary delineation. After guiding the F_{SAM} , we further refine the resulting feature map F_{fused} using the semantic prior vector T_{attr} constructed during the cognitive stage. The refine process can be formulated as follows:

$$F_{\text{sem}} = \text{MHCA}_C(F_{\text{fused}}, F_{\text{attr}}, F_{\text{attr}}), \quad (4)$$

where MHCA_C denotes multi-head cross-attention along the channel dimension following Yin et al. [2024].

4 Experiments

4.1 Experimental setup

Datasets. We evaluate MedSeg-R on SA-Med2D-20M and Synapse. SA-Med2D-20M Cheng et al. [2023] contains multi-modality medical images with dense segmentation masks. Following SEG-

Table 1: Comparisons between our MedSeg-R and other state-of-the-art SAM-based methods on the Med2D-16M dataset. We use Dice to evaluate the binary medical segmentation performance. ‘*’ indicates the experimental results we reproduced.

Prompt	Method	CT	MR	PET	Dermoscopy	Endoscopy	Funds	US	X-ray	Average
point	SAM* Kirillov et al. [2023]	30.27	23.18	36.31	36.90	32.46	32.81	19.31	20.31	28.97
	SAM2* Ravi et al. [2024]	63.81	44.18	71.36	83.41	58.33	74.06	64.77	46.11	63.25
	SAM-Med2D* Cheng et al. [2023]	71.44	48.35	73.00	86.40	59.41	76.06	65.00	49.41	66.13
	MedSAM* Ma et al. [2024]	73.00	51.51	68.91	87.33	55.80	77.39	69.09	53.71	67.09
	Med-SA* Wu et al. [2025]	73.51	46.92	73.71	89.41	60.11	77.91	66.01	42.73	66.29
	SEG-SAM* Huang et al. [2024]	78.35	53.81	77.31	88.05	69.16	80.52	71.07	60.00	72.28
	MedSeg-R (Ours)	80.32	58.91	79.45	90.24	70.74	80.94	72.00	61.53	74.27
box	SAM* Kirillov et al. [2023]	63.61	51.62	63.73	84.13	70.30	77.70	77.38	52.52	67.62
	SAM2* Ravi et al. [2024]	79.41	59.31	77.41	90.58	78.40	86.37	85.59	61.47	77.32
	SAM-Med2D* Cheng et al. [2023]	81.42	61.72	79.44	92.71	77.37	87.41	85.37	59.25	78.09
	MedSAM* Ma et al. [2024]	83.18	63.27	77.24	90.89	74.16	84.25	85.15	64.25	77.80
	Med-SA* Wu et al. [2025]	83.46	61.79	80.11	92.83	77.35	85.81	84.19	57.72	77.86
	SEG-SAM* Huang et al. [2024]	85.74	65.71	81.41	91.35	80.84	84.86	85.73	70.16	80.73
	MedSeg-R (Ours)	86.61	66.94	82.49	92.51	81.73	85.72	87.42	71.74	81.90

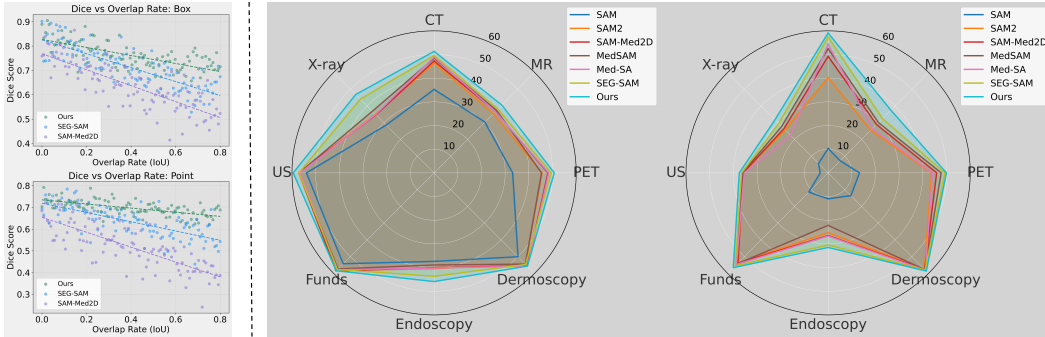


Figure 3: Combined analysis of anatomical overlap robustness (left) and small-object segmentation (right). **Left:** Dice versus overlap rate under box prompts (top) and point prompts (bottom). MedSeg-R shows the weakest negative correlation and the flattest regression slope, indicating superior resilience to inter-class ambiguity. **Right:** Radar charts of per-modality Dice scores under box prompts (left) and point prompts (right). MedSeg-R consistently outperforms SEG-SAM and other baselines across all eight modalities, with the greatest improvements in challenging, low-contrast domains such as ultrasound and dermoscopy.

SAM Huang et al. [2024], we use eight representative modalities for point/box-prompt evaluation. All modalities are trained on a 25% subset and tested on the full test set. To assess generalization without prompts, we also report results on Synapse, a CT dataset with pixel-level annotations for eight abdominal organs.

Implementation Details. All models are trained for 50 epochs on eight RTX 3090 GPUs using the AdamW optimizer ($\beta_1=0.9$, $\beta_2=0.999$, weight decay = 0.1). Input images are uniformly resized to 224×224 pixels, with a per-GPU batch size of 12.

4.2 Comprehensive Evaluation on the SAM-Med2D Dataset

We compare MedSeg-R with seven leading SAM-based segmentation methods on the SAM-Med2D benchmark to assess the benefits of early integration of structured priors, namely location, texture, and shape. Our evaluation focuses on three aspects: (1) prompt-based performance, (2) robustness to anatomical overlap, and (3) segmentation of very small targets across eight imaging modalities.

Prompt-based performance. We first assess performance under point prompts. Results in the upper half of Table 1 show that MedSeg-R achieves an average dice score of **74.27%**, outperforming SEG-SAM (72.28%) by **+1.99%**. Notably, our method leads across all modalities, with the largest improvements observed in MR (+5.10%) and X-ray (+1.53%). This indicates that even minimal spatial cues can be greatly amplified by structured semantic priors. Next, we evaluate the models under box prompts, which provide more precise spatial constraints. As shown in the lower half of Table 1, MedSeg-R achieves an average Dice score of **81.90%**, surpassing SEG-SAM (80.73%) by **+1.17%**. This improvement further confirms that stronger localization enables more effective

Table 2: Comparisons with state-of-the-art models on the Synapse multi-organ CT dataset in both few-shot and fully-supervised settings. Greyed values represent our results. mDice: the Mean Dice coefficient; HD95: the 95th percentile of the Hausdorff Distance. ‘*’ indicates the experimental results we reproduced.

Method		Spleen	Kidney (R)	Kidney (L)	Gallbladder	Liver	Stomach	Aorta	Pancreas	mDice ↑	HD95 ↓
Non-SAM	TransUnet Chen et al. [2021]	87.23	63.13	81.87	77.02	94.08	55.86	85.08	75.62	77.48	31.69
	SwinUnet Cao et al. [2022]	85.47	66.53	83.28	79.61	94.29	56.58	90.66	76.60	79.13	21.55
	TransDeepLab Azad et al. [2022]	86.04	69.16	84.08	79.88	93.53	61.19	89.00	78.40	80.16	21.25
	DAE-Former Azad et al. [2023]	88.96	72.30	86.08	80.88	94.98	65.12	91.94	79.19	82.43	17.46
	MERIT Rahman and Marculescu [2024]	92.01	84.85	87.79	74.40	95.26	85.38	87.71	71.81	84.90	13.22
SAM	AutoSAM Hu et al. [2023]	80.54	80.02	79.66	41.37	89.24	61.14	82.56	44.22	62.08	27.56
	SAM Adapter Chen et al. [2023]	83.68	79.00	79.02	57.49	92.68	69.48	77.93	43.07	72.80	33.08
	SAMed Zhang and Liu [2023]	87.33	80.10	82.75	70.24	93.37	73.62	86.99	67.64	80.26	28.89
	H-SAM Cheng et al. [2024]	92.34	85.99	87.71	69.65	95.20	86.27	87.53	72.53	84.65	7.29
	PG-SAM Zhong et al. [2025]	93.12	84.57	87.93	73.26	95.40	86.62	87.87	71.49	84.79	7.61
	SEG-SAM*	92.10	84.16	86.39	70.21	94.91	86.06	87.42	71.48	84.09	10.26
	MedSeg-R (Ours)	93.49	86.70	89.71	78.29	95.17	87.77	88.91	73.71	86.71	6.13

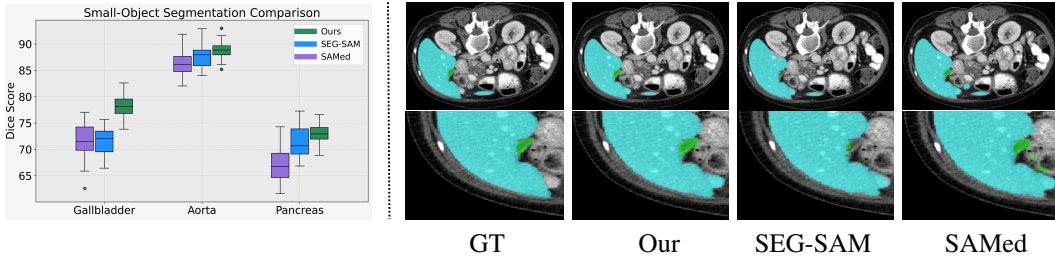


Figure 4: **Left:** Box plot of dice scores for three small volume organs, gallbladder, pancreas, and aorta, on the Synapse dataset. Each distribution compares MedSeg-R, SEG-SAM, and SAMed under identical settings, with MedSeg-R showing consistently higher medians and tighter spreads, highlighting its superior sensitivity to small-object segmentation amid class imbalance and anatomical overlap. **Right:** Segmentation results on the Synapse dataset, showing masks of the gallbladder (green) and liver (blue) generated by different methods, illustrating the improved boundary delineation of MedSeg-R. illustrating MedSeg-R’s improved boundary delineation.

exploitation of structural priors. Overall, MedSeg-R consistently leverages both sparse and dense prompts to deliver enhanced segmentation accuracy across all eight modalities.

Robustness to anatomical overlap. Adjacent anatomical structures often exhibit high visual similarity and spatial proximity, causing inter-class ambiguity and performance degradation. To quantify robustness, we analyze the correlation between Dice scores and overlap rates for three representative models: MedSeg-R, SEG-SAM, and SAM-Med2D, under both box and point prompts. Results are shown in the left of Fig. 3. Under the **box** prompt, MedSeg-R exhibits the smallest performance drop, with a Pearson correlation of approximately $r \approx -0.36$ and a regression slope of -0.12 . In comparison, SEG-SAM yields $r \approx -0.58$ (slope -0.23), and SAM-Med2D shows $r \approx -0.70$ (slope -0.36). With the **point** prompt, all methods suffer more due to sparse guidance. However, MedSeg-R remains most robust, with $r \approx -0.45$ and slope -0.15 , compared to SEG-SAM ($r \approx -0.68$, slope -0.29) and SAM-Med2D ($r \approx -0.75$, slope -0.43). These consistently weaker negative correlations and shallower slopes confirm the strong ability of MedSeg-R to handle overlapping anatomies, validating the effectiveness of early semantic-prior integration.

Small object segmentation. Segmenting objects that occupy less than 5% of the image area is particularly challenging due to severe class imbalance and limited pixel support. We systematically evaluate small object performance across eight modalities, using radar plots under both box and point prompts, as shown on the right of Fig. 3. Under box prompts, MedSeg-R achieves an average Dice score of **51.33%**, outperforming SEG-SAM (49.57%) by **+1.76%**, with the largest improvement observed in ultrasound (+2.43%) and dermoscopy (+1.60%). With point prompts, it attains **59.10%**, ahead of SEG-SAM (57.41%) by **+1.69%**. These results highlight the ability of MedSeg-R to maintain high sensitivity to small structures, effectively overcoming challenges posed by overlap and class imbalance. The radar visualization underscores the consistency and robustness of our approach across diverse imaging modalities.

Table 3: Ablation study of structured semantics at the cognitive stage. We evaluate the individual and combined contributions of location, texture, and shape. "Loc." and "Tex." denote location and texture. Results are reported as Dice scores on the KiTS19 and Kvasir datasets. Best results are highlighted in gray.

Loc.	Tex.	Shape	KiTS19	Kvasir
			77.21	76.46
✓			83.91	83.39
	✓		82.99	82.96
		✓	82.25	82.07
✓	✓		86.38	85.71
✓		✓	85.14	84.34
	✓	✓	85.81	84.69
✓	✓	✓	88.23	87.69

Table 4: Ablation study of structured semantic priors at the perceptual stage. We evaluate the individual and combined contributions of location, texture, and shape priors. "Loc." and "Tex." denote location and texture. Results are reported as Dice scores on the KiTS19 and Kvasir datasets. Best results are highlighted in gray.

Loc. prior	Tex.prior	Shape prior	KiTS19	Kvasir
			80.39	84.01
✓			85.97	85.31
	✓		85.09	84.74
		✓	83.79	84.11
✓	✓		87.77	86.99
✓		✓	87.39	86.59
	✓	✓	86.01	84.89
✓	✓	✓	88.23	87.69

4.3 Evaluation on Synapse: Multi-Organ CT Segmentation.

To assess the performance of MedSeg-R in fully automatic segmentation settings, we do experiments on the Synapse dataset, which contains contrast-enhanced abdominal CT scans annotated for eight organ types. Unlike previous evaluations relying on point or box prompts, this prompt-free setup enables direct evaluation of the model’s intrinsic segmentation capability without external guidance.

Overall segmentation performance. We compare MedSeg-R with several state-of-the-art fully supervised and SAM-based methods, including SEG-SAM, H-SAM, and PG-SAM. As shown in Table 2, MedSeg-R achieves the highest mean Dice score of **86.71%** and the lowest HD95 of **6.13**, outperforming SEG-SAM (84.09%) by **+2.62%** and PG-SAM (84.79%) by **+1.92%**. Notably, our method yields consistent improvements for all organs, with substantial gains on anatomically challenging structures, such as the **gallbladder** (+5.03%) and **pancreas** (+2.22%). These results demonstrate the sustained effectiveness of early-integrated structured semantic priors, even in scenarios without user guidance.

Robustness to anatomical overlap. To evaluate the performance in spatially entangled regions, we examine organ pairs known for strong anatomical overlap and boundary ambiguity, including *gallbladder-liver*, *pancreas-stomach*, and *kidney-aorta*. These structures are prone to inter-class confusion due to partial occlusion and weak boundary contrast. As shown in Table 2, MedSeg-R consistently outperforms competing methods on challenging structures, achieving Dice scores of 78.29% for the gallbladder, 73.71% for the pancreas, and 87.77% for the stomach. This indicates that our semantic guidance mechanism enhances spatial discrimination and improves robustness in complex anatomical environments.

Small object segmentation. Although the Synapse dataset primarily contains medium-to-large abdominal organs, structures such as the **gallbladder**, **pancreas**, and **aorta** remain particularly challenging due to their small spatial extent, high class imbalance, and frequent boundary overlap with neighboring tissues. We designate these organs as representative small structures and illustrate their segmentation performance using box plots shown on the left of Fig. 4.

MedSeg-R achieves both the highest median Dice scores and the most compact performance distributions for all three organs, outperforming SEG-SAM by +8.08% on the gallbladder, +2.23% on the pancreas, and +1.49% on the aorta. These results demonstrate the model’s enhanced sensitivity to small anatomical targets and its robustness under limited pixel supervision and inter-class interference. The right of Fig. 4 further illustrates the benefits of structured semantic guidance. The figure compares segmentation results across methods for the gallbladder. MedSeg-R achieves clearer boundary delineation and more accurate mask alignment, underscoring the effectiveness of early semantic prior integration in small object segmentation.

Table 5: Ablation on the effectiveness of the cognitive stage (Cog.), perceptual stage (Per.), and cross-attribute attention (CAA) in MedSeg-R. We examine their individual and combined contributions on KiTS19 and Kvasir datasets. ‘CAA’ denotes the cross-attribute attention module used within the cognitive stage. Results are reported as dice scores on the KiTS19 and Kvasir datasets. Best results are highlighted in gray.

Cog.	Per.	CAA	KiTS19	Kvasir
			77.21	76.46
✓			80.39	84.01
✓	✓		86.05	85.20
✓	✓		88.23	87.69
✓	✓		87.22	86.14
✓	✓	✓	88.23	87.69

Table 6: Ablation study on the gating mechanism for feature fusion. We evaluate the individual and combined effects of three feature branches: the perceptually guided feature F_{fused} , the cognitively refined feature F_{sem} , and the raw feature from SAM F_{sam} . The results are reported in terms of dice score on the KiTS19 and Kvasir datasets. Best performance is highlighted in gray.

F_{fused}	F_{sem}	F_{sam}	KiTS19	Kvasir
✓			85.03	84.15
	✓		85.91	84.67
		✓	85.60	84.40
✓	✓		86.71	85.69
✓		✓	86.11	85.31
	✓	✓	87.30	86.72
✓	✓	✓	88.23	87.69

4.4 Ablation Study

We perform extensive ablation experiments to validate the effectiveness of the proposed modules, including structured semantic priors, the two-stage architecture, cross-attribute attention, and the gating mechanism. All results are reported as Dice scores on the KiTS19 and Kvasir datasets.

Effect of structured semantics at the cognitive stage. Table 3 analyzes the impact of structured semantics (location, texture, and shape) when incorporated at the cognitive stage. Each type of semantic prior individually improves performance over the baseline (77.21 / 76.46). Among them, location priors contribute the most (83.91 / 83.39), while texture and shape bring moderate gains. Combining two types of priors leads to further improvements, and the best performance (88.23 / 87.69) is achieved when all three priors are jointly used.

Effect of structured semantics at the perceptual stage. As shown in Table 4, introducing structured priors into the perceptual stage also consistently improves performance. Location priors again play a dominant role (85.97 / 85.31). Combining two priors shows stronger results, and the full combination of all priors leads to the best performance (88.23 / 87.69). This indicates that structured semantics can also effectively guide low-level visual representation learning.

Effectiveness of the two-stage framework and cross-attribute attention. We further evaluate the contribution of the cognitive stage, the perceptual stage, and the cross-attribute attention (CAA) in Table 5. Removing both stages leads to the lowest performance (77.21 / 76.46). Enabling either stage improves results, with the perceptual stage providing stronger gains than the cognitive stage. Combining both stages achieves the highest score (88.23 / 87.69), confirming their complementarity. Notably, the introduction of CAA brings a clear improvement (from 87.22 / 86.14 to 88.23 / 87.69), demonstrating its ability to facilitate interaction between diverse structured priors.

Analysis on the gating mechanism. Finally, Table 6 investigates the contribution of each feature branch and their combinations in the fusion stage. The fused feature F_{fused} , cognitively refines the feature F_{sem} , and the SAM feature F_{sam} , each individually improving performance over the baseline. Combining any two of them further enhances accuracy, and the full gating of all three features yields the best performance (88.23 / 87.69). This confirms the effectiveness of the gating mechanism in selectively integrating complementary information from multiple feature streams.

5 Conclusions

In this work, we present MedSeg-R, a structured semantic attribute-guided framework that enhances SAM’s segmentation capabilities in the presence of small lesions and inter-class anatomical overlap. By introducing position-, texture-, and shape-aware guidance into the feature encoding and fusion process, MedSeg-R enables more precise delineation of subtle lesion boundaries and im-

proves robustness in structurally ambiguous regions. Comprehensive experiments across multi-organ and lesion-centric benchmarks demonstrate that our method outperforms existing SAM-based and universal segmentation baselines, particularly in low-contrast and imbalanced settings.

Limitations. While our method integrates structured priors to improve segmentation robustness, these priors are still learned implicitly from data rather than being explicitly encoded. As a result, the model may struggle to fully adapt to patient-specific anatomical variations or rare pathological patterns. This challenge is common across existing SAM-based frameworks. However, MedSeg-R demonstrates stronger resilience in such scenarios by incorporating a clinically inspired reasoning mechanism, leading to improved generalization compared to prior approaches. Future work could incorporate explicit clinical knowledge or case-specific adaptation to further enhance robustness to rare or out-of-distribution cases.

References

- Reza Azad, Moein Heidari, Moein Shariatnia, Ehsan Khodapanah Aghdam, Sanaz Karimijafarbigloo, Ehsan Adeli, and Dorit Merhof. Transdeeplab: Convolution-free transformer-based deeplab v3+ for medical image segmentation. In *International Workshop on Predictive Intelligence In Medicine*, pages 91–102. Springer, 2022. 7
- Reza Azad, René Arimond, Ehsan Khodapanah Aghdam, Amirhossein Kazerouni, and Dorit Merhof. Dae-former: Dual attention-guided efficient transformer for medical image segmentation. In *International workshop on predictive intelligence in medicine*, pages 83–95. Springer, 2023. 7
- Victor Ion Butoi, Jose Javier Gonzalez Ortiz, Tianyu Ma, Mert R Sabuncu, John Guttag, and Adrian V Dalca. Universeg: Universal medical image segmentation. In *Proceedings of the IEEE/CVF International Conference on Computer Vision*, pages 21438–21451, 2023. 2, 3
- Hu Cao, Yueyue Wang, Joy Chen, Dongsheng Jiang, Xiaopeng Zhang, Qi Tian, and Manning Wang. Swin-unet: Unet-like pure transformer for medical image segmentation. In *European conference on computer vision*, pages 205–218. Springer, 2022. 3, 7
- Jieneng Chen, Yongyi Lu, Qihang Yu, Xiangde Luo, Ehsan Adeli, Yan Wang, Le Lu, Alan L Yuille, and Yuyin Zhou. Transunet: Transformers make strong encoders for medical image segmentation. *arXiv preprint arXiv:2102.04306*, 2021. 1, 3, 7
- Peijie Chen, Qi Li, Saad Biaz, Trung Bui, and Anh Nguyen. gscorecam: What objects is clip looking at? In *Proceedings of the Asian Conference on Computer Vision*, pages 1959–1975, 2022. 3
- Tianrun Chen, Lanyun Zhu, Chaotao Ding, Runlong Cao, Yan Wang, Zejian Li, Lingyun Sun, Papa Mao, and Ying Zang. Sam fails to segment anything?—sam-adapter: Adapting sam in underperformed scenes: Camouflage, shadow, medical image segmentation, and more. *arXiv preprint arXiv:2304.09148*, 2023. 7
- Junlong Cheng, Jin Ye, Zhongying Deng, Jianpin Chen, Tianbin Li, Haoyu Wang, Yanzhou Su, Ziyang Huang, Jilong Chen, Lei Jiang, et al. Sam-med2d. *arXiv preprint arXiv:2308.16184*, 2023. 2, 3, 5, 6, 13, 14, 15
- Zhiheng Cheng, Qingyue Wei, Hongru Zhu, Yan Wang, Liangqiong Qu, Wei Shao, and Yuyin Zhou. Unleashing the potential of sam for medical adaptation via hierarchical decoding. In *Proceedings of the IEEE/CVF Conference on Computer Vision and Pattern Recognition*, pages 3511–3522, 2024. 7
- Özgün Çiçek, Ahmed Abdulkadir, Soeren S Lienkamp, Thomas Brox, and Olaf Ronneberger. 3d u-net: learning dense volumetric segmentation from sparse annotation. In *Medical Image Computing and Computer-Assisted Intervention—MICCAI 2016: 19th International Conference, Athens, Greece, October 17–21, 2016, Proceedings, Part II 19*, pages 424–432. Springer, 2016. 3
- Jifeng Dai, Haozhi Qi, Yuwen Xiong, Yi Li, Guodong Zhang, Han Hu, and Yichen Wei. Deformable convolutional networks. In *Proceedings of the IEEE international conference on computer vision*, pages 764–773, 2017. 5
- Yuhang Ding, Liulei Li, Wenguan Wang, and Yi Yang. Clustering propagation for universal medical image segmentation. In *Proceedings of the IEEE/CVF conference on computer vision and pattern recognition*, pages 3357–3369, 2024. 3
- Nicolás Gaggion, Lucas Mansilla, Candelaria Mosquera, Diego H Milone, and Enzo Ferrante. Improving anatomical plausibility in medical image segmentation via hybrid graph neural networks: applications to chest x-ray analysis. *IEEE Transactions on Medical Imaging*, 42(2):546–556, 2022. 1

- Yunhe Gao, Di Liu, Zhuowei Li, Yunsheng Li, Dongdong Chen, Mu Zhou, and Dimitris N Metaxas. Show and segment: Universal medical image segmentation via in-context learning. *arXiv preprint arXiv:2503.19359*, 2025. 3
- Xuan Gong, Xin Xia, Wentao Zhu, Baochang Zhang, David Doermann, and Li'an Zhuo. Deformable gabor feature networks for biomedical image classification. In *Proceedings of the IEEE/CVF Winter Conference on applications of computer vision*, pages 4004–4012, 2021. 5
- Xinrong Hu, Xiaowei Xu, and Yiyu Shi. How to efficiently adapt large segmentation model (sam) to medical images. *arXiv preprint arXiv:2306.13731*, 2023. 7
- Chao Huang, Hu Han, Qingsong Yao, Shankuan Zhu, and S Kevin Zhou. 3d u 2-net: A 3d universal u-net for multi-domain medical image segmentation. In *International Conference on Medical Image Computing and Computer-Assisted Intervention*, pages 291–299. Springer, 2019. 3
- Shuangping Huang, Hao Liang, Qingfeng Wang, Chulong Zhong, Zijian Zhou, and Miaoqing Shi. Seg-sam: Semantic-guided sam for unified medical image segmentation. *arXiv preprint arXiv:2412.12660*, 2024. 2, 6, 13
- Shahzaib Iqbal, Tariq M Khan, Syed S Naqvi, Asim Naveed, Muhammad Usman, Haroon Ahmed Khan, and Imran Razzak. Ldmres-net: A lightweight neural network for efficient medical image segmentation on iot and edge devices. *IEEE journal of biomedical and health informatics*, 28(7):3860–3871, 2023. 1
- Fabian Isensee, Jens Petersen, Andre Klein, David Zimmerer, Paul F Jaeger, Simon Kohl, Jakob Wasserthal, Gregor Koehler, Tobias Norajitra, Sebastian Wirkert, et al. nnu-net: Self-adapting framework for u-net-based medical image segmentation. *arXiv preprint arXiv:1809.10486*, 2018. 3
- Alexander Kirillov, Eric Mintun, Nikhila Ravi, Hanzi Mao, Chloe Rolland, Laura Gustafson, Tete Xiao, Spencer Whitehead, Alexander C Berg, Wan-Yen Lo, et al. Segment anything. In *Proceedings of the IEEE/CVF international conference on computer vision*, pages 4015–4026, 2023. 6, 14, 15
- Taha Koleilat, Hojat Asgariandehkordi, Hassan Rivaz, and Yiming Xiao. Medclip-sam: Bridging text and image towards universal medical image segmentation. In *International Conference on Medical Image Computing and Computer-Assisted Intervention*, pages 643–653. Springer, 2024. 3
- Wenxue Li, Xinyu Xiong, Peng Xia, Lie Ju, and Zongyuan Ge. Tp-drseg: improving diabetic retinopathy lesion segmentation with explicit text-prompts assisted sam. In *International Conference on Medical Image Computing and Computer-Assisted Intervention*, pages 743–753. Springer, 2024. 3
- Yuheng Li, Yuxiang Lai, Maria Thor, Deborah Marshall, Zachary Buchwald, David S Yu, and Xiaofeng Yang. Towards universal text-driven ct image segmentation. *arXiv preprint arXiv:2503.06030*, 2025. 3
- Jun Ma, Yao Zhang, Song Gu, Xingle An, Zhihe Wang, Cheng Ge, Congcong Wang, Fan Zhang, Yu Wang, Yinan Xu, et al. Fast and low-gpu-memory abdomen ct organ segmentation: the flare challenge. *Medical Image Analysis*, 82:102616, 2022. 1
- Jun Ma, Yuting He, Feifei Li, Lin Han, Chenyu You, and Bo Wang. Segment anything in medical images. *Nature Communications*, 15(1):654, 2024. 2, 6, 14, 15
- Ozan Oktay, Jo Schlemper, Loic Le Folgoc, Matthew Lee, Mattias Heinrich, Kazunari Misawa, Kensaku Mori, Steven McDonagh, Nils Y Hammerla, Bernhard Kainz, et al. Attention u-net: Learning where to look for the pancreas. *arXiv preprint arXiv:1804.03999*, 2018. 1, 3
- Md Mostafjuz Rahman and Radu Marculescu. Multi-scale hierarchical vision transformer with cascaded attention decoding for medical image segmentation. In *Medical Imaging with Deep Learning*, pages 1526–1544. PMLR, 2024. 7
- Nikhila Ravi, Valentin Gabeur, Yuan-Ting Hu, Ronghang Hu, Chaitanya Ryali, Tengyu Ma, Haitham Khedr, Roman Rädle, Chloe Rolland, Laura Gustafson, et al. Sam 2: Segment anything in images and videos. *arXiv preprint arXiv:2408.00714*, 2024. 6, 14
- Olaf Ronneberger, Philipp Fischer, and Thomas Brox. U-net: Convolutional networks for biomedical image segmentation. In *Medical image computing and computer-assisted intervention—MICCAI 2015: 18th international conference, Munich, Germany, October 5-9, 2015, proceedings, part III 18*, pages 234–241. Springer, 2015. 1, 3
- Bas Schipaanboord, Djamel Boukerroui, Devis Peressutti, Johan van Soest, Tim Lustberg, Andre Dekker, Wouter van Elmpt, and Mark J Gooding. An evaluation of atlas selection methods for atlas-based automatic segmentation in radiotherapy treatment planning. *IEEE transactions on medical imaging*, 38(11):2654–2664, 2019. 1

- Hao Shao, Yang Zhang, and Qibin Hou. Polyper: Boundary sensitive polyp segmentation. In *Proceedings of the AAAI conference on artificial intelligence*, volume 38, pages 4731–4739, 2024. 1
- Ashish Vaswani, Noam Shazeer, Niki Parmar, Jakob Uszkoreit, Llion Jones, Aidan N Gomez, Łukasz Kaiser, and Illia Polosukhin. Attention is all you need. *Advances in neural information processing systems*, 30, 2017. 3
- Haoyu Wang, Sizheng Guo, Jin Ye, Zhongying Deng, Junlong Cheng, Tianbin Li, Jianpin Chen, Yanzhou Su, Ziyang Huang, Yiqing Shen, et al. Sam-med3d: towards general-purpose segmentation models for volumetric medical images. *arXiv preprint arXiv:2310.15161*, 2023. 3
- Wang Wenxuan, Chen Chen, Ding Meng, Yu Hong, Zha Sen, and Li Jiangyun. Transbts: Multimodal brain tumor segmentation using transformer. In *International Conference on Medical Image Computing and Computer-Assisted Intervention, Springer*, pages 109–119, 2021. 3
- Junde Wu, Ziyue Wang, Mingxuan Hong, Wei Ji, Huazhu Fu, Yanwu Xu, Min Xu, and Yueming Jin. Medical sam adapter: Adapting segment anything model for medical image segmentation. *Medical image analysis*, 102:103547, 2025. 3, 6
- Yutong Xie, Jianpeng Zhang, Chunhua Shen, and Yong Xia. Cotr: Efficiently bridging cnn and transformer for 3d medical image segmentation. In *Medical Image Computing and Computer Assisted Intervention–MICCAI 2021: 24th International Conference, Strasbourg, France, September 27–October 1, 2021, Proceedings, Part III 24*, pages 171–180. Springer, 2021. 3
- Yiwen Ye, Yutong Xie, Jianpeng Zhang, Ziyang Chen, and Yong Xia. Uniseg: A prompt-driven universal segmentation model as well as a strong representation learner. In *International Conference on Medical Image Computing and Computer-Assisted Intervention*, pages 508–518. Springer, 2023. 2, 3
- Bowen Yin, Xuying Zhang, Deng-Ping Fan, Shaohui Jiao, Ming-Ming Cheng, Luc Van Gool, and Qibin Hou. Camoformer: Masked separable attention for camouflaged object detection. *IEEE Transactions on Pattern Analysis and Machine Intelligence*, 2024. 5
- Kaidong Zhang and Dong Liu. Customized segment anything model for medical image segmentation. *arXiv preprint arXiv:2304.13785*, 2023. 7
- Wenjie Zhang, Ziyang Zhang, Mengnan He, and Jiancheng Ye. Organ-aware multi-scale medical image segmentation using text prompt engineering. *arXiv preprint arXiv:2503.13806*, 2025. 3
- Sixiao Zheng, Jiachen Lu, Hengshuang Zhao, Xiatian Zhu, Zekun Luo, Yabiao Wang, Yanwei Fu, Jianfeng Feng, Tao Xiang, Philip HS Torr, et al. Rethinking semantic segmentation from a sequence-to-sequence perspective with transformers. In *Proceedings of the IEEE/CVF conference on computer vision and pattern recognition*, pages 6881–6890, 2021. 1, 3
- Yiheng Zhong, Zihong Luo, Chengzhi Liu, Feilong Tang, Zelin Peng, Ming Hu, Yingzhen Hu, Jionglong Su, Zongyuan Geand, and Imran Razzak. Pg-sam: Prior-guided sam with medical for multi-organ segmentation. *arXiv preprint arXiv:2503.18227*, 2025. 7
- Zongwei Zhou, Md Mahfuzur Rahman Siddiquee, Nima Tajbakhsh, and Jianming Liang. Unet++: A nested u-net architecture for medical image segmentation. In *Deep learning in medical image analysis and multimodal learning for clinical decision support: 4th international workshop, DLMIA 2018, and 8th international workshop, ML-CDS 2018, held in conjunction with MICCAI 2018, Granada, Spain, September 20, 2018, proceedings 4*, pages 3–11. Springer, 2018. 3

A Appendix

A.1 Overview

In this appendix, we provide additional results and details to supplement the main paper. The content is organized as follows:

- **Dataset and Implementation Details:** In Sec. A.2, we include further information on dataset partitioning and pre-processing protocols, as well as key training settings such as optimizer parameters.
- **Structured Semantic Attribute Extraction:** In Sec. A.3, we describe the process for extracting structured semantic attributes from medical reports generated by LLM.

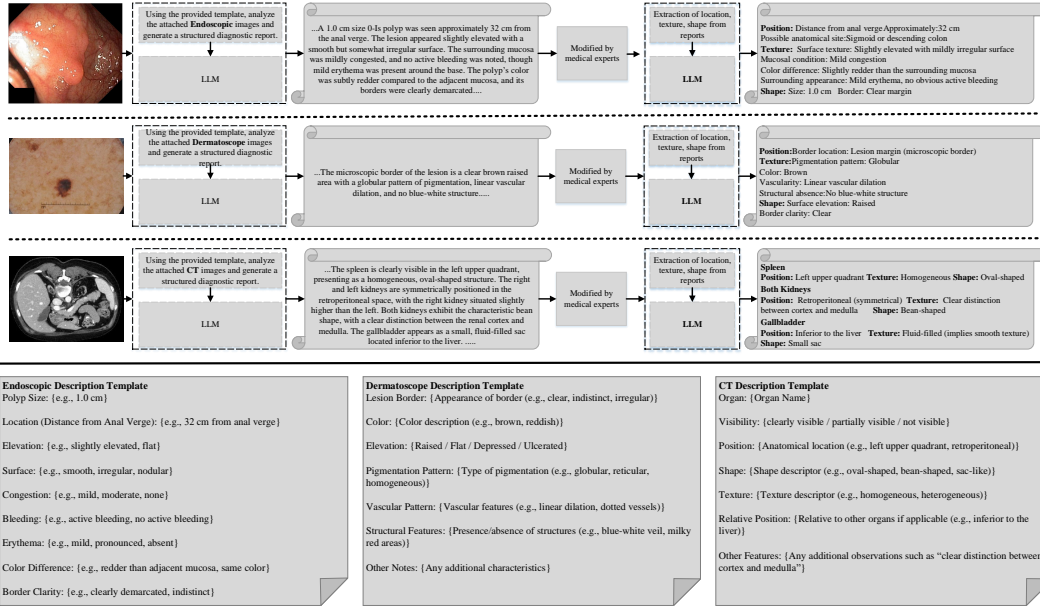


Figure 5: An illustration of the process for extracting structured semantic attributes from medical images across three modalities: CT, endoscopy, and dermoscopy. The **upper** part of the figure shows the pipeline from image input to language-based attribute extraction. The **lower** part of the figure demonstrates how prompts are constructed based on the input image, which are then used by the LLM to generate the medical report.

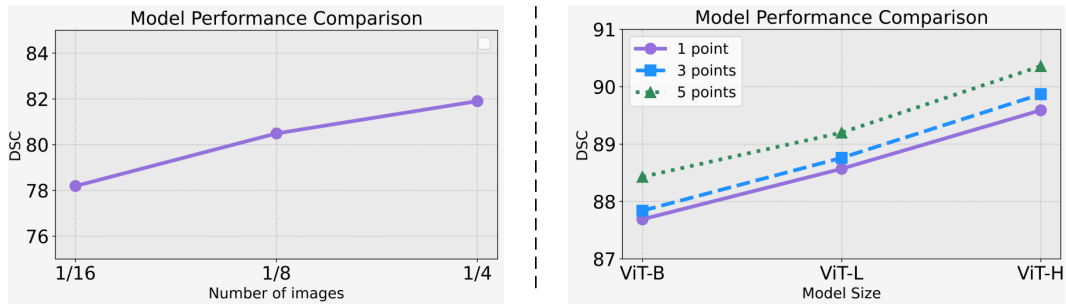


Figure 6: Impact of data volume and prompt strategy on performance. **Left:** Comparison of model performance under different training data volumes (e.g., 1/16, 1/8, and 1/4). **Right:** Evaluation across model scales (ViT-B, ViT-H, ViT-L) with varying point-based prompts (e.g., 1-point, 2-points, and 3-points). Our method exhibits consistent gains with increased model capacity.

- **Computational Efficiency Comparison:** In Sec. A.4, We present quantitative results on model efficiency in terms of trainable parameter counts and inference speed (FPS), demonstrating the advantage of our design.
- **Ablation Studies:** In Sec. A.5, additional experiments are conducted to evaluate the impact of dataset size, model capacity, and the number of point prompts on segmentation performance.
- **Visualization Results:** In Sec. A.6, additional segmentation results across various modalities are presented to further demonstrate the effectiveness and generalizability of MedSeg-R.

A.2 Experiment setup

Datasets. We report the results on SA-Med2D-20M and Synapse. SA-Med2D-20M introduced by SAM-Med2D Cheng et al. [2023] contains 4.6 million medical images paired with approximately 20 million segmentation masks spanning ten imaging modalities. In line with SEG-SAM Huang et al.

Table 7: Comparison of tuned parameters and inference speed (FPS) among SAM-based segmentation methods. MedSeg-R (Ours) achieves significantly higher FPS than most baselines while reducing the number of trainable parameters, demonstrating the efficiency of our structured semantic guidance.

Method	Model	Tuned Params(M)	FPS
SAM Kirillov et al. [2023]	ViT-B	89.88	8
SAM2 Ravi et al. [2024]	hiera-base-plus	80.8	64.8
SAM-Med2D Cheng et al. [2023]	ViT-B	163	35
MedSAM Ma et al. [2024]	ViT-B	93.73	13
MedSeg-R (Ours)	ViT-B	68.49	48

[2024], we select eight clinically representative modalities for our point- and box-prompt experiments: CT, MR, PET, US, X-ray, endoscopy, dermoscopy, and fundus. All data are divided into 80% for training and 20% for testing. Due to computational constraints, both the MedSeg-R and baseline models are trained on a randomly sampled 25% subset of the training data, while the evaluation is performed on the entire test dataset. To evaluate the generalizability of MedSeg-R under prompt-free conditions, we further conduct experiments on the Synapse dataset. This dataset comprises 3,779 contrast-enhanced abdominal CT slices with pixel-wise annotations for eight major organs, offering a consistent single-modality setting. Unlike SA-Med2D-20M, no prompts are provided during training or inference, enabling us to rigorously assess segmentation performance—particularly in anatomically complex and small object scenarios.

Implementation Details. All models are trained for 50 epochs on eight RTX 3090 GPUs using the AdamW optimizer ($\beta_1=0.9$, $\beta_2=0.999$, weight decay = 0.1). Input images are uniformly resized to 224×224 pixels, with a per-GPU batch size of 12. We follow the data pre-processing strategy of SAM-Med2D Cheng et al. [2023]. For 3D images, all slices along the three orthogonal axes are extracted and treated as independent 2D samples. For 2D images, we normalize pixel values to the range [0, 255]. To reduce label noise, we discard ground truth masks occupying less than 0.153% of the image area, as they are too small to extract meaningful features.

A.3 Extracting Structured Semantic Attributes

The pipeline for extracting structured semantic attributes is illustrated in Fig. 5. Given an input image (e.g., CT, endoscopy, or dermoscopy), a large language model (LLM) is first employed to generate a preliminary descriptive medical report. This report is subsequently reviewed and refined by medical experts to ensure clinical accuracy and consistency. The revised report is then re-processed by the LLM to extract fine-grained semantic attributes, specifically the position, texture, and shape of relevant anatomical or pathological structures. These structured attributes serve as lightweight yet informative priors that can be seamlessly integrated into downstream segmentation or diagnostic models, enhancing both interpretability and generalizability across imaging modalities.

A.4 Computational efficiency

To evaluate computational efficiency, we compare our method MedSeg-R with representative SAM-based models in terms of the number of tuned parameters and inference speed (FPS), as shown in Table 7. While the original SAM Kirillov et al. [2023] and MedSAM Ma et al. [2024] fine-tune a large number of parameters (over 89M), our method freezes the SAM backbone and only tunes structured semantic guidance and mask decoder, resulting in a significantly smaller trainable parameter count (68.49M). In addition, MedSeg-R achieves an inference speed of 48 FPS, outperforming MedSAM (13 FPS) and SAM-Med2D (35 FPS). These results highlight the efficiency of our approach in balancing performance and computational cost, making it more suitable for real-time or resource-constrained clinical applications.

A.5 Ablation study

Impact of Dataset Size on Model Performance. To assess the effect of training data volume on model performance, we conduct experiments using different proportions of the SAM-Med2D dataset, specifically 1/16, 1/8, and 1/4 of the training dataset. As shown in the left of Fig. 6, model performance—as measured by Dice Similarity Coefficient (DSC)—increases steadily with the number

of training images. Even with only 1/16 of the data, our model achieves a DSC of 78.19%, and this performance rises to 81.90% when trained on 1/4 of the dataset. These results highlight the scalability of our approach and its ability to effectively learn from increasing amounts of training data, without any changes to supervision strategies.

Effect of Model Size and Prompt Quantity on Segmentation Performance. We evaluate the performance of models with different capacities (ViT-B, ViT-L, ViT-H) under varying numbers of point prompts (1, 3, and 5) using the SAM-Med2D dataset. As shown in the right of Fig. 6, while larger models consistently yield better segmentation results—as measured by Dice Similarity Coefficient (DSC)—the performance improvement from increasing the number of prompts is relatively modest across all model sizes. For instance, ViT-H achieves a DSC of 89.59% with a single point, and only improves to 90.36% with five points. This trend suggests that our model is capable of generating accurate segmentation with minimal user input, demonstrating strong robustness even in low-prompt or prompt-free scenarios. This property makes the model particularly suitable for real-world clinical settings where extensive annotation is often impractical.

A.6 Visualization results

To qualitatively assess the segmentation capability of MedSeg-R across diverse imaging modalities, we present representative results on three different types of medical images: computed tomography (CT), dermoscopy, and endoscopy. These modalities differ significantly in terms of anatomical structures, visual appearance, and imaging conditions, providing a rigorous evaluation of the generalizability of our approach.

As shown in Fig. 7, Fig. 8, and Fig. 9, our method produces accurate and consistent segmentation masks across all three modalities. For CT images, MedSeg-R is able to delineate organ boundaries with high precision, even in cases with low contrast or ambiguous edges. In dermoscopic images, which often exhibit high intra-class variation and low inter-class contrast, our method captures the fine-grained lesion structures while preserving clear margins. Similarly, in endoscopic scenarios, where occlusions, lighting variations, and texture complexity pose significant challenges, MedSeg-R demonstrates robust performance in segmenting irregular and often small anatomical targets.

These results highlight the strong adaptability of our method to both multi-modality (Fig. 8 and Fig. 9) and prompt-free (Fig. 7) settings. Importantly, the structured semantic priors incorporated into MedSeg-R contribute to more anatomically plausible predictions, especially in visually complex scenes where traditional prompt-driven models often struggle. We also provide visual comparisons with representative baselines, including SAM Kirillov et al. [2023], SAM-Med2D Cheng et al. [2023], and MedSAM Ma et al. [2024], to further substantiate the effectiveness of MedSeg-R.

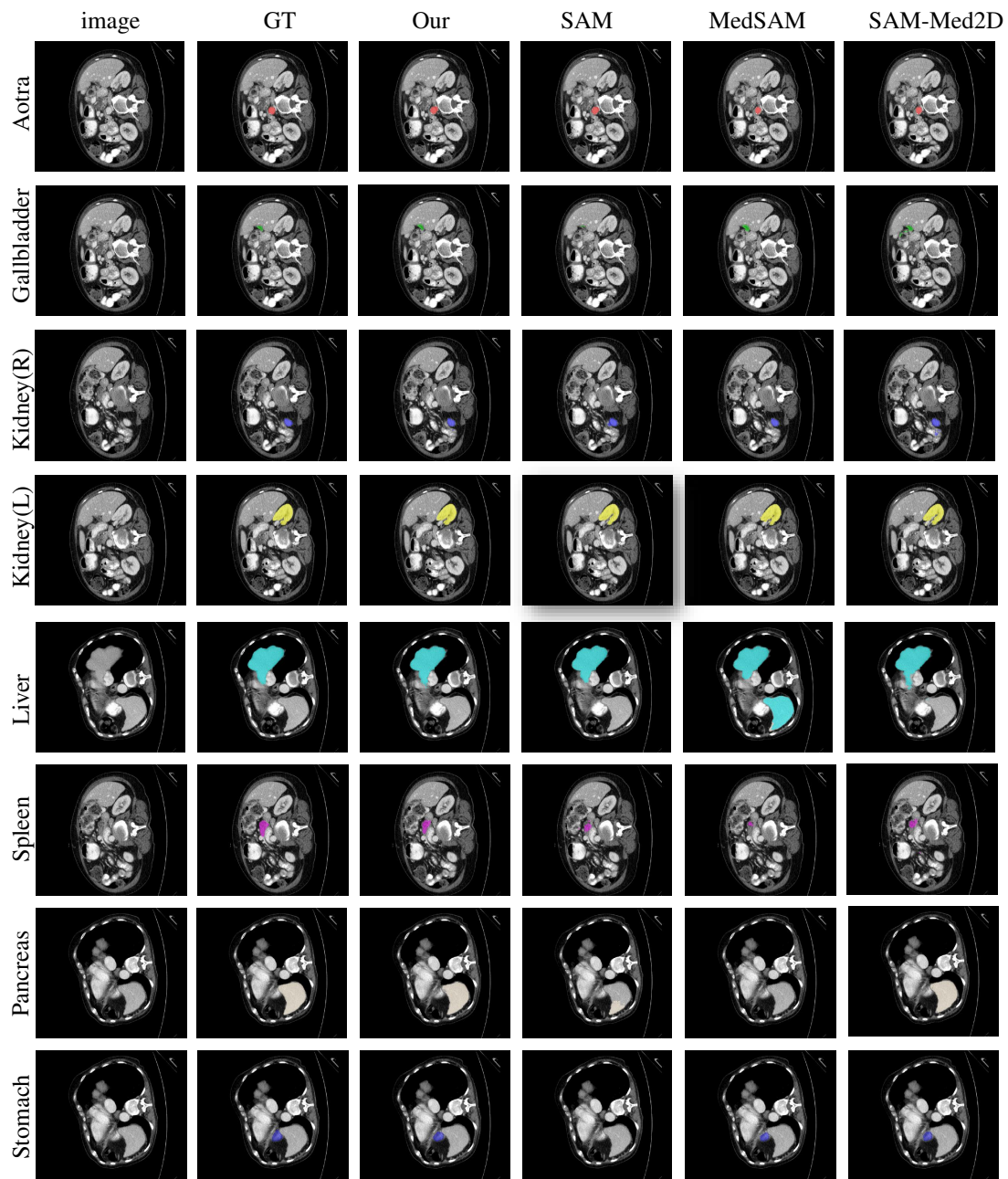


Figure 7: Segmentation results of different methods on the Synapse dataset.

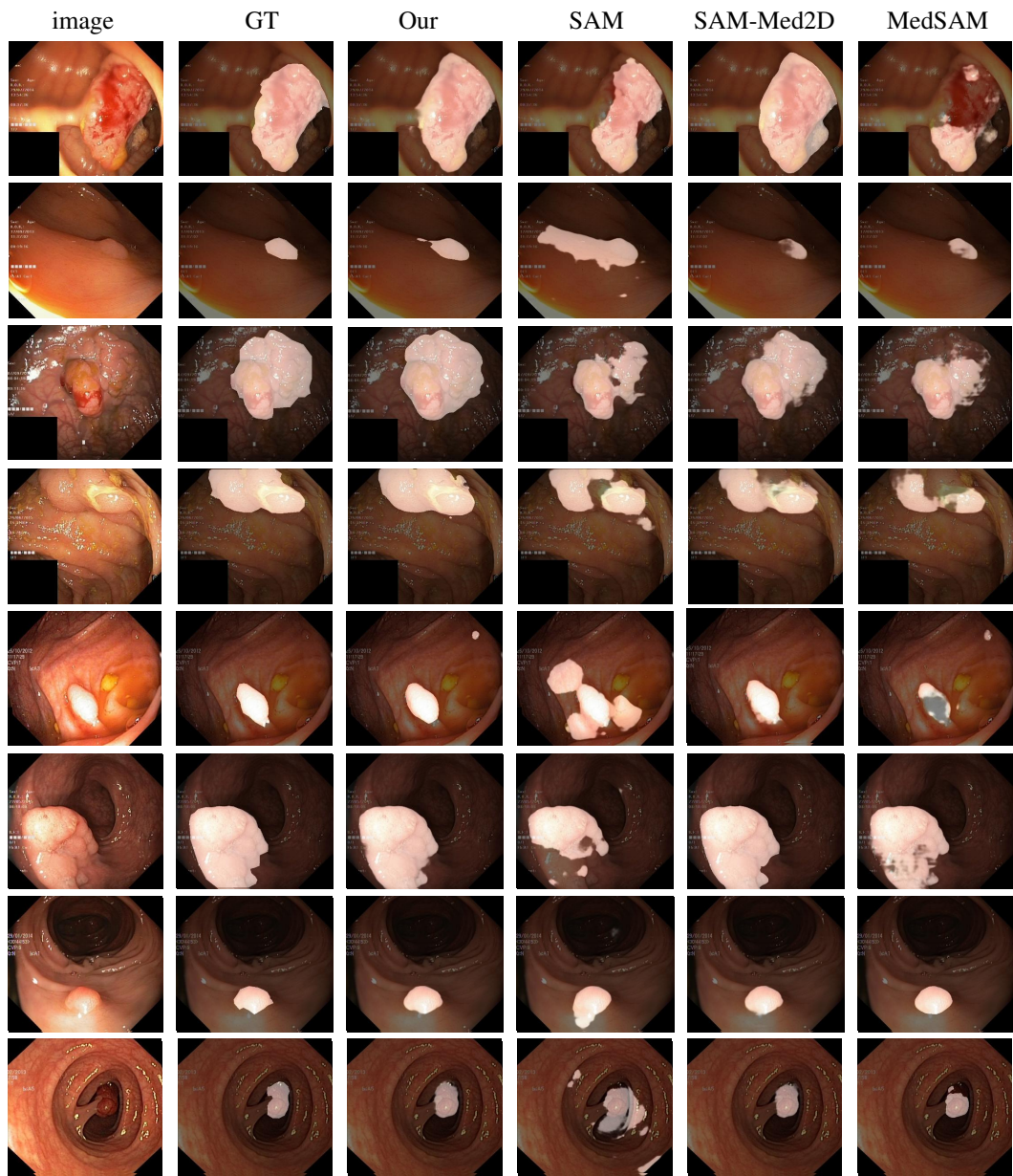


Figure 8: Segmentation results of different methods on the Endoscopy modality.

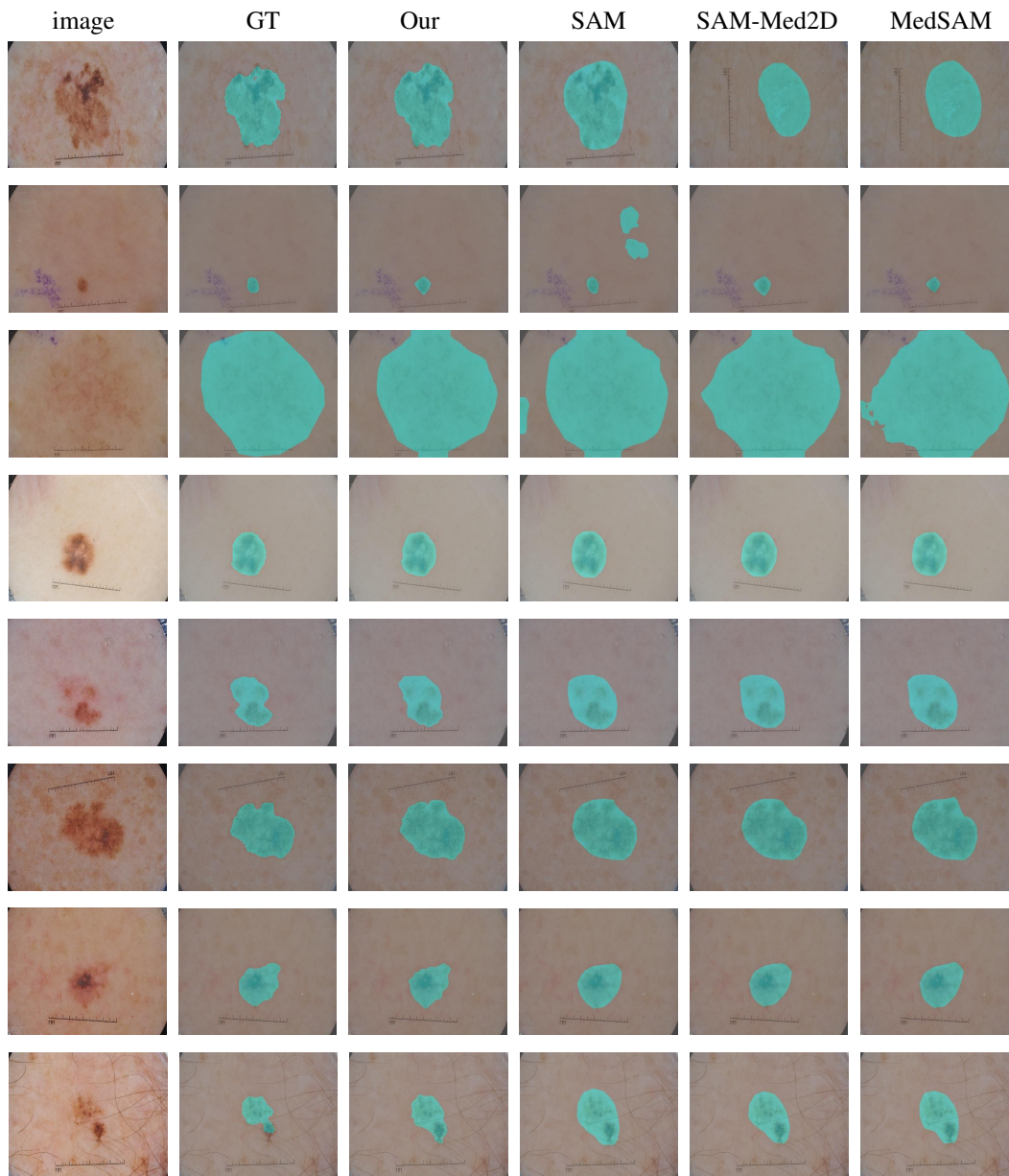


Figure 9: Segmentation results of different methods on the Derscopy modality.